The Astrophysical Journal, 977:215 (9pp), 2024 December 20 https://doi.org/10.3847/1538-4357/ad93b0

AstroSat View of the Neutron Star Low-mass X-Ray Binary GX 5-1

V. P. Shyam Prakash[1,2] and Vivek K. Agrawal[1]
[1] Space Astronomy Group, ISITE Campus, U. R. Rao Satellite Center, ISRO, Bengaluru 560037, India; shyamvp151@gmail.com
[2] Department of Physics, University of Calicut, Kerala 673635, India
Received 2024 March 22; revised 2024 November 13; accepted 2024 November 14; published 2024 December 16

Abstract

We present the spectral and timing study of the bright neutron star low-mass X-ray binary GX 5-1 using AstroSat/Large Area X-ray Proportional Counter (LAXPC) and Soft X-ray Telescope observations conducted in 2018. During the observation, the source traces out the complete horizontal branch (HB) and normal branch (NB) of the Z-track in the hardness–intensity diagram (HID). Understanding the spectral and temporal evolution of the source along the Z-track can probe the accretion process in the vicinity of a neutron star. Spectral analysis was performed in the 0.7–20 keV energy range for different segments in the HID using a multitemperature disk blackbody with an average temperature, $kT_{\rm in} \sim 0.47$, and a thermal Comptonization model. It is found that the optical depth of the corona drops from ∼7.07 in HB to ∼2.61 in NB. The timing analysis using the LAXPC instrument indicates the presence of quasiperiodic oscillations in HB and NB of the Z-track. The observed QPO frequencies are similar to the characteristic frequencies of horizontal branch oscillations (HBOs) and normal branch oscillations (NBOs). The HBO frequency increases from ∼12 to 40 Hz toward the hard apex. NBOs are observed at ∼5 Hz. The timing studies conducted in soft and hard bands indicate the association of HBO and NBO origin with the nonthermal component. Further research could explore the implications of this relationship for understanding the dynamics of accretion onto neutron stars.

Unified Astronomy Thesaurus concepts: X-ray astronomy (1810); Low-mass x-ray binary stars (939); Neutron stars (1108); Compact objects (288)

1. Introduction

X-ray binaries are a class of objects that consist of a compact object, a black hole or a neutron star, and an optical companion star (N. I. Shakura & R. A. Sunyaev 1973) that emits X-ray radiation. Depending on the ratio of X-ray to optical luminosity and the mass of the companion star, X-ray binaries can be classified into low-mass X-ray binaries (LMXBs) and high-mass X-ray binaries. In neutron star LMXBs, the compact object is a neutron star, and the mass of the companion star is less than or equal to solar mass. In such a binary system, neutron stars accrete matter from a companion star by Roche-lobe overflow through the inner Lagrangian point (T. M. Tauris & E. P. J. van den Heuvel 2006). They have a relatively low surface magnetic field and spin periods compared to other binary systems. LMXBs are further classified into "Z" and "atoll" sources based on the patterns they trace in the hardness–intensity diagram (HID) and color–color diagram (G. Hasinger & M. van der Klis 1989). An "atoll" source traces a banana and island state in its HID. In Z sources, a change in the mass accretion rate is considered to be the reason for tracing the Z pattern in the HID (G. Hasinger & M. van der Klis 1989; M. P. Muno et al. 2003; J. Homan et al. 2007).

Various models were proposed to explain the continuum spectrum of LMXB systems. One of the most important is the eastern model, which comprises a multicolor blackbody emission from the accretion disk and a Comptonized emission from the close regions of the neutron star (K. Mitsuda et al. 1989). The western model (N. E. White et al. 1988) suggests a blackbody emission component from a boundary layer present between the neutron star and the accretion disk. Both the eastern and western models take into account the hot plasma that can produce a hard X-ray spectrum. Reflection features, if present in the spectra (e.g., R. R. Ross et al. 1999), can provide more information on the changes in accretion flow along the Z-track. An Fe K_α line around 6.4 keV due to fluorescence (K. Asai et al. 2000) and a reflection hump observed between 10 and 30 keV (M. Fiocchi et al. 2007) due to Compton backscattering can be present. Both of these features result from the irradiation of the inner accretion disk and are sensitive to changes in accretion geometry. J. Homan et al. (2018) have discussed the absence of the K_α line in the NuSTAR spectrum of GX 5-1.

Quasiperiodic oscillations (QPOs) are observed as peaks in the power density spectrum (PDS) of the source, which is characterized both by a centroid frequency and its width. The properties of these oscillations shown by the source are highly dependent on the position within the HID. QPOs observed in the HB are termed horizontal branch oscillations (HBOs). It has a characteristic frequency in the range of 15–60 Hz (R. Wijnands et al. 1998). Normal branch oscillations (NBOs) are seen in the normal branch of the Z-track at a much shorter frequency (5–7 Hz; M. van der Klis 2004). Apart from these branch oscillations, millisecond and kilohertz QPOs have also been detected in many LMXBs (see R. Wijnands et al. 1998; P. G. Jonker et al. 2000; M. van der Klis 2000), with most of the kilohertz QPOs displaying twin peaks. There have been many attempts in the past to explain the origin of these features, but it is still unclear.

GX 5-1 is a persistent neutron star LMXB, discovered in 1968 (H. Bradt et al. 1968; P. C. Fisher et al. 1968). Further, it is classified as a "Z" source as it traces a Z pattern in its HID (G. Hasinger & M. van der Klis 1989). It is the second-brightest persistent LMXB located in the direction of the

Galactic center. It has luminosity close to Eddington luminosity ($L/L_{\rm Edd}$) = 1.6–2.3). It is also considered a Cygnus-like source because it shows a short flaring branch (FB) and an extended horizontal branch (HB; E. Kuulkers et al. 1994). The source has exhibited NBOs and HBOs along with kHz QPOs in the past (M. van der Klis et al. 1985; R. Wijnands et al. 1998). A model for Z-track in the source was studied earlier using RXTE data by N. K. Jackson et al. (2009). The variable energy-dependent X-ray polarization in the source has been studied by S. Fabiani et al. (2024). Y. Bhulla et al. (2019) have studied the source using AstroSat observations conducted in the year 2017. Anticorrelated soft and hard lags were detected in the source using AstroSat data by P. Chiranjeevi & K. Sriram (2022). A review by F. Capitanio et al. (2023) explains that the polarization signatures from the source are highly correlated with the position in the HID, with maximum polarization in the HB.

Even decades after the first studies of the evolution of the Z-track in LMXB sources, the cause of this evolution is not clearly understood. In this work, we attempt a broadband spectral and timing study of the Cyg-like Z source GX 5-1 using AstroSat data. The observations cover the entire HB and NB of the Z-track. The broadband spectral capability and good timing resolution of the LAXPC instrument on AstroSat help us investigate the spectral and temporal evolution of the source throughout different states along the Z-track.

The paper is organized as follows: The details of the observations and the data reduction are provided in Section 2. Details of the spectral and temporal analyses are presented in Section 3. The observations and findings from the analysis are given in Section 4. Finally, we discuss the results from the present study in Section 5.

2. Observation and Data Reduction

AstroSat has observed the LMXB source, GX 5-1, several times from 2018 February to May using the LAXPC (H. M. Antia et al. 2017) and Soft X-ray Telescope (SXT; K. P. Singh et al. 2017) instruments with observation IDs `G08_068T01_9000001922` and `G08_068T01_9000002090` with an effective exposure time of ∼42 ks. Observations were conducted for LAXPC in event mode and for SXT in photon counting mode. Simultaneous observational data from these instruments are used for spectral analysis. Out of the three LAXPC instruments, LAXPC10 and LAXPC30 exhibited anomalous behaviors, including gain change and gas leakage. For this investigation, we used archived data from the LAXPC20 instrument. The source traces most of the Z-track during the observation, except the FB. We reduced the LAXPC data using `laxpcsoftv3.4.3_07May2022`[3] developed by the Tata Institute of Fundamental Research. Level 1 data are converted to Level 2 using the software for generating scientific products. The software also includes calibration files and responses. The Good Time Interval (GTI) file is generated, and the light curves and spectra are extracted from the Level 2 files.

SXT data reduction was carried out using the SXT software. Photon counting mode data were merged using the SXT Event Merger Tool[4] and used the merged event file to extract the image. The source counts were extracted from a circular region of radius 15′, and a region of radius 3′ was excluded from the center to avoid pileup issues. The SXT region selection for the extraction of source counts is shown in Figure 1. The latest available redistribution matrix file (sxt_pc_mat_g0to12.rmf) and background (SkyBkg_comb_EL3p5_Cl_Rd16p0_v01.pha) files were used during analysis. The ancillary response file (ARF) was created using the SXTARFModule tool[5] after correcting for the vignetting effect.

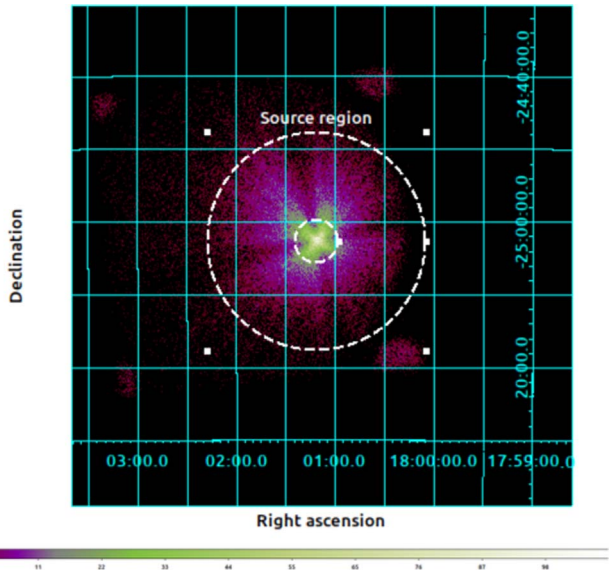

Figure 1. SXT image of the source in the 0.7–7 keV energy band. The annular region used to extract the source counts to generate light curves and spectra is also shown.

3. Analysis

3.1. HID

We investigate the evolution of the source during the period of observation by plotting the HID. Data from the LAXPC20 instrument were used for plotting the HID with 3–8 and 8–20 keV as the soft and hard energy bands, respectively, as shown in Figure 2. Each point in the figure corresponds to the intensity and hardness ratio values for the 256 s binned light curve. The source traces most of its Z-track during these observations, except for the FB. An extended HB is observed in the HID. For a detailed understanding of the evolution of spectral and temporal properties along the branches, we split the HID into six segments: three segments in HB and three in NB. To extract the segment-resolved spectral and light-curve products, we identified the GTI files for each of the segments and used these files for product extraction. Spectral files and PDS are generated from each segment for further analysis.

3.2. Timing Analysis

For timing analysis, only the data from the LAXPC20 instrument were considered. The evolution of QPO properties of the source along different branches was studied using PDS extracted in the energy range of 3–30 keV up to a maximum frequency of 100 Hz. Higher frequencies were excluded because the PDS above 100 Hz was dominated by Poisson noise. We calculated the rms-normalized PDS (T. Belloni et al. 2002) for each segment. Dead-time-corrected Poisson noise level is subtracted from the PDS (W. Zhang et al. 1995;

[3] https://www.tifr.res.in/astrosat_laxpc/software.html
[4] https://www.tifr.res.in/astrosat_sxt/dataanalysis.html
[5] https://www.tifr.res.in/astrosat_sxt/dataanalysis.html

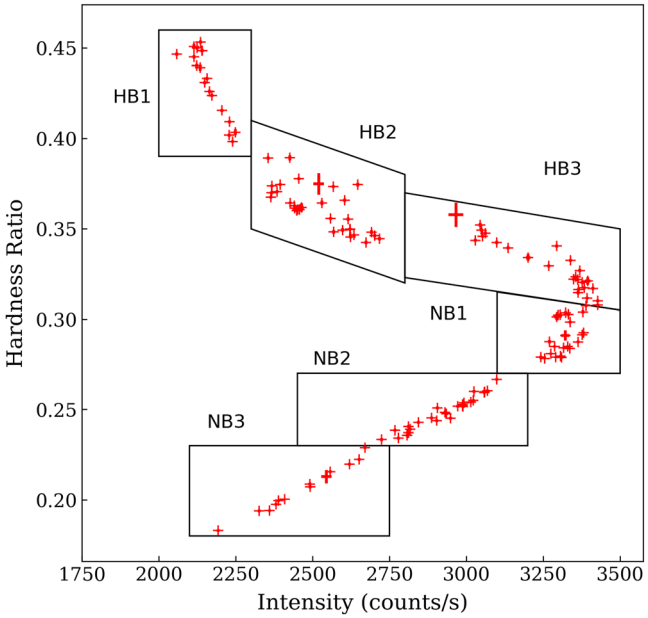

Figure 2. The hardness–intensity diagram (HID) of the source GX 5-1 plotted using data from LAXPC20 with hard color computed using the count rates in 8–20 keV divided by that in 3–8 keV and intensity represented by the total counts in 3–20 keV. Boxes represent the regions considered for segment-based spectral and timing analysis.

V. K. Agrawal et al. 2018). An instrumental peak around 50 Hz has been observed in the LAXPC20 instrument and is attributed to the noise in the amplifier for anode A1 in LAXPC20 (H. M. Antia et al. 2017). To account for this, we ignored frequencies close to 50 Hz from the PDS. The PDS was modeled using multiple Lorentzian and power-law functions. QPOs and the band-limited noise (BLN) features in the PDS are modeled using the Lorentzian function (T. Belloni et al. 2002) defined as

$$A(E) = K(\sigma/2\pi)/[(\nu - \nu_L)^2 + (\sigma/2)^2]. \quad (1)$$

A Lorentzian model is characterized by three features: the centroid frequency (ν_L) gives the position of the QPO signal in the PDS, the normalization (K), and the FWHM of the signal (σ). The very low-frequency noise (VLFN) features in the PDS were modeled using a power-law function ($A\nu^{-\alpha}$) with normalization A and index α. The BLN features with a low value of ν_L are referred to as the low-frequency (LF) noise. We detect the presence of QPOs in five out of the six segments considered. The quality factor (Q) is defined as the ratio of centroid frequency to the FWHM of the QPO signal, and the rms amplitude, which is the measure of the strength of the QPO signal, was also calculated. We also report $\nu_{\rm max}$, the highest frequency covered by the Lorentzian component (T. Belloni et al. 2002):

$$\nu_{\rm max} = \sqrt{\nu_L^2 + (\sigma/2)^2} \quad (2)$$

This is the frequency at which the Lorentzian contributes most of its power per logarithmic frequency interval. The best-fit parameters of power spectral components in the different segments of the Z-track are reported in Table 1. PDSs are generated in soft (3–4.5 keV) and hard (4.5–20.0 keV) energy bands to understand the dependence of the observed QPO features on energy. We find that the QPOs are observed only in PDS generated for the hard energy band, giving a strong connection between the origin of the QPOs and the high-energy emission mechanism.

3.3. Spectral Analysis

Spectral fitting is carried out in the broad energy range of 0.7–20.0 keV by combining the data from LAXPC and SXT instruments. For SXT, 0.7–7.0 keV and 3.0–20.0 keV energy ranges for LAXPC are considered. We restricted the LAXPC energy range up to 20.0 keV due to the dominance of the background in the spectrum. We fitted the spectrum in six distinct segments in the HID using `XSPEC` version 12.0. We attempted two phenomenological spectral models to fit the X-ray spectrum of the source in all segments. First, we modeled the spectrum with the combination of a blackbody emission component from boundary layer/NS surface (`bbodyrad` model in `XSPEC`) and a thermal Comptonized emission from the corona (`nthComp`), which is called Model 1. In Model 2, we replaced the blackbody emission with emission from a multicolor disk. The best-fit parameters are reported in Tables 2 and 3, respectively. Both models provide a statistically preferred fit; however, Model 2 was adopted as the best model because of the low reduced χ^2 values observed in all segments. The spectra could be well described by the multicolor disk blackbody model `diskbb` (K. Mitsuda et al. 1984), along with the thermally Comptonized continuum emission model `nthComp` (P. T. Zycki et al. 1999). For absorption along the line of sight, the `XSPEC` model `Tbabs` (J. Wilms et al. 2000) was used. The hydrogen column density $N_{\rm H}$ was fixed at the best-fit value of 2.7×10^{22} cm^{-2}, and a systematic error of 3% was added during the spectral fitting. The final model used for the fitting is `tbabs*(diskbb+nthComp)`. Spectral parameters are noted in each segment, and their evolution across different segments is plotted in Figure 5. The best-fit parameters are discussed in Table 3 with 1σ error of measurements. Reflection features such as Fe K_α or Compton hump were absent in the spectrum.

4. Results

The broadband spectral analysis of GX 5-1 has been carried out using the AstroSat SXT and LAXPC20 instruments. The temporal properties of the source have been studied using data from the LAXPC20 instrument. The HID of the source traces the HB and NB branches of the Z pattern. The broadband spectrum in the energy range 0.7–20.0 keV was used to understand the spectral properties and estimate various physical parameters of the source. The simultaneous SXT and LAXPC spectrum could be modeled using the `tbabs*(diskbb +nthComp)` model in `XSPEC`. The best-fit values of the spectral parameters are given in Table 3, and the spectral fit in all segments considered are shown in Figure 3. In this section, we discuss the findings and our understanding of the source behavior.

4.1. Estimation of Physical Parameters

We derive key parameters, such as inner disk radius and optical depth, for the spectrum in each segment from spectral fitting. The normalization of the blackbody component of the disk gives us an estimate of the inner radius of the accretion

Table 1
The Best-fit Parameters Obtained by Fitting the PDS in Different Segments of the Z-track

Parameters	HB1	HB2	HB3	NB1	NB2	NB3
			QPO Lorentzian			
ν_{max} (Hz)	12.3 ± 0.1	32.6 ± 0.7	40.3 ± 1.2	4.5 ± 0.3	5.8 ± 0.2	⋯
σ (Hz)	1.4 ± 0.2	5.1 ± 2.4	10.8 ± 3.5	1.6 ± 0.4	3.4 ± 0.7	⋯
LN ($\times 10^{-4}$)	2.2 ± 0.3	5.4 ± 3.4	6.8 ± 1.3	41.5 ± 11.4	6.2 ± 0.8	⋯
rms (%)	4.7 ± 0.3	2.3 ± 0.7	2.6 ± 0.3	6.4 ± 0.9	2.5 ± 0.2	⋯
			LF Noise (Lorentzian)			
ν_{max} (Hz)	0[a]	0[a]	0[a]	2.0 ± 0.3	⋯	⋯
σ (Hz)	5.2 ± 0.4	6.1 ± 0.3	11 ± 3	1.7 ± 0.5	⋯	⋯
LN ($\times 10^{-3}$)	6.7 ± 0.5	8.5 ± 0.3	1.7 ± 0.2	6.5 ± 1.7	⋯	⋯
			Power Law (VLFN)			
α	1.2 ± 0.2	1.5 ± 1.0	1.1 ± 0.2	2.1 ± 1.0	1.7 ± 0.4	1.9 ± 0.5
Norm ($\times 10^{-4}$)	3.5 ± 1.1	0.8 ± 0.2	1.3 ± 0.5	3.0 ± 0.3	0.3 ± 0.1	0.4 ± 0.2
			Additional Lorentzian 1			
ν_{max} (Hz)	14.1 ± 0.1	26.3 ± 0.5	⋯	14.2 ± 0.4	⋯	⋯
σ (Hz)	1.3 ± 0.6	6.8 ± 0.6	⋯	2.7 ± 0.7	⋯	⋯
LN ($\times 10^{-3}$)	8.5 ± 4.3	3.1 ± 0.3	⋯	0.6 ± 0.1	⋯	⋯
rms (%)	2.9 ± 0.7	5.6 ± 0.2	⋯	2.5 ± 0.2	⋯	⋯
			Additional Lorentzian 2			
ν_{max} (Hz)	16.3 ± 0.5	⋯	⋯	24.1 ± 0.6	⋯	⋯
σ (Hz)	8.7 ± 1.0	⋯	⋯	1.9 ± 1.5	⋯	⋯
LN ($\times 10^{-3}$)	5.2 ± 0.7	⋯	⋯	0.1 ± 0.1	⋯	⋯
rms (%)	7.2 ± 0.5	⋯	⋯	1.2 ± 0.3	⋯	⋯
			Additional Lorentzian 3			
ν_{max} (Hz)	⋯	⋯	⋯	48 ± 4	⋯	⋯
σ (Hz)	⋯	⋯	⋯	20[a]	⋯	⋯
LN ($\times 10^{-4}$)	⋯	⋯	⋯	5.6 ± 1.2	⋯	⋯
rms (%)	⋯	⋯	⋯	2.4 ± 0.3	⋯	⋯
χ^2/dof	148/108	155/122	78/115	98/107	136/119	102/119

Notes. The integrated rms in the 0.1–100 Hz is also provided.
[a] Represents frozen parameters.

Table 2
Best-fit Spectral Parameter Values Along with Their 1σ Error Values for the Individual Segments in the HID for 3–20 keV Energy Band Combining LAXPC and SXT Spectrum

Fitted parameters	HB1	HB2	HB3	NB1	NB2	NB3
kT (keV)	$1.3^{+0.1}_{-0.1}$	$1.31^{+0.05}_{-0.05}$	$1.25^{+0.03}_{-0.03}$	$1.15^{+0.05}_{-0.05}$	$1.16^{+0.03}_{-0.03}$	$1.11^{+0.03}_{-0.03}$
$N_{bbodyrad}$ ($\times 10^2$)	$1.2^{+0.3}_{-0.3}$	$2.1^{+0.4}_{-0.4}$	$4.2^{+0.5}_{-0.4}$	$4.8^{+1.1}_{-0.9}$	$9.1^{+1.0}_{-1.1}$	$9.4^{+1.1}_{-1.3}$
Γ	$1.77^{+0.04}_{-0.06}$	$1.8^{+0.1}_{-0.1}$	$1.7^{+0.1}_{-0.1}$	$2.2^{+0.1}_{-0.2}$	$1.8^{+0.1}_{-0.1}$	$2.1^{+0.1}_{-0.1}$
kT_e (keV)	$3.2^{+0.2}_{-0.2}$	$3.2^{+0.1}_{-0.2}$	$3.0^{+0.1}_{-0.1}$	$3.2^{+0.1}_{-0.1}$	$2.8^{+0.1}_{-0.1}$	$2.8^{+0.2}_{-0.1}$
kT_{bb} (keV)	$0.4^{+0.1}_{-0.1}$	$0.6^{+0.1}_{-0.2}$	$0.5^{+0.1}_{-0.2}$	$1.4^{+0.2}_{-0.3}$	$0.6^{+0.2}_{-0.3}$	0.84[a]
N_{nth}	$1.3^{+0.1}_{-0.1}$	$1.25^{+0.1}_{-0.1}$	$1.3^{+0.1}_{-0.1}$	$1.1^{+0.2}_{-0.2}$	$1.2^{+0.2}_{-0.3}$	$1.92^{+0.2}_{-0.2}$
χ^2/dof	871/645	969/649	890/651	850/651	859/651	772/629

Notes. The model used for fitting is tbabs*(bbodyrad+nthComp).
[a] Represents frozen parameters.

disk. It is given by the relation

$$\text{Norm} = \left(\frac{R_{in}}{D_{10}}\right)^2 \cos\theta, \quad (3)$$

where D_{10} is the distance to the source in units of 10 kpc and θ is the inclination of the disk. The Monte Carlo simulation of the X-ray halos of GX 5-1 suggests that the approximate distance to the source is 4.2 kpc (G. W. Clark 2018). We see that the radius is approximately in the range of 35–55 km in all the segments and shows an increase along the HB. To calculate the disk radius, we assume an inclination of 60° for the source. This assumption is based on the absence of dips or eclipses in its light curve, as noted

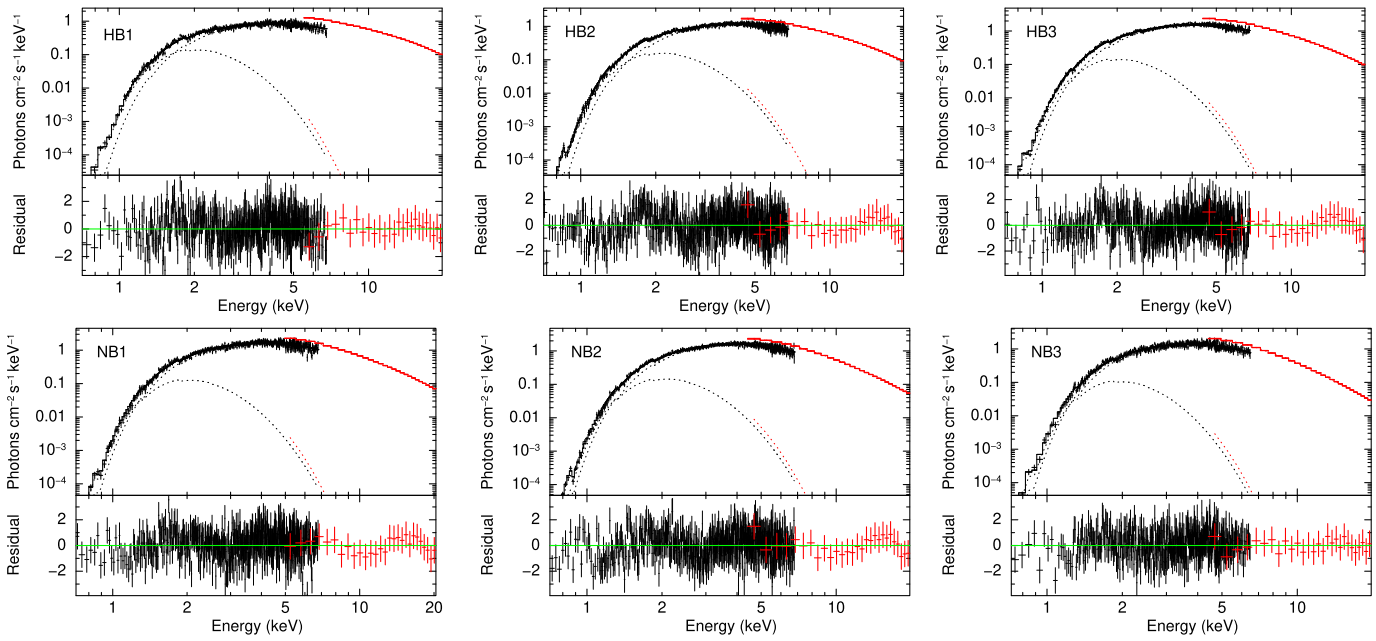

Figure 3. GX 5-1 spectrum in HB and NB fitted using the model `tbabs*(diskbb+nthComp)` in the 3–20 keV energy band. Residuals are also plotted along with the fit.

Table 3
Best-fit Spectral Parameter Values Along with Their 1σ Error Values for the Individual Segments in the HID for 3–20 keV Energy Band Combining LAXPC and SXT Spectrum

Fitted Parameters	HB1	HB2	HB3	NB1	NB2	NB3
$kT_{\rm in}$ (keV)	$0.44^{+0.04}_{-0.04}$	$0.49^{+0.04}_{-0.04}$	$0.44^{+0.03}_{-0.04}$	$0.44^{+0.05}_{-0.07}$	$0.46^{+0.05}_{-0.05}$	$0.40^{+0.06}_{-0.08}$
$N_{\rm diskbb}$ ($\times10^3$)	$5.8^{+1.9}_{-3.1}$	$3.6^{+1.1}_{-1.6}$	$6.1^{+1.9}_{-2.8}$	$5.4^{+2.5}_{-4.7}$	$4.8^{+1.8}_{-2.9}$	$8.5^{+4.8}_{-11}$
Γ	$2.3^{+0.1}_{-0.1}$	$2.7^{+0.2}_{-0.2}$	$3.0^{+0.2}_{-0.2}$	$3.2^{+0.2}_{-0.3}$	$3.7^{+0.3}_{-0.4}$	$3.9^{+0.3}_{-0.4}$
kT_e (keV)	$3.8^{+0.3}_{-0.4}$	$4.6^{+0.6}_{-1.0}$	$5.0^{+0.7}_{-1.5}$	$5.1^{+0.8}_{-1.8}$	$6.8^{+1.9}_{-8.8}$	$6.1^{+1.5}_{-5.9}$
$kT_{\rm bb}$ (keV)	$0.93^{+0.06}_{-0.06}$	$1.05^{+0.04}_{-0.05}$	$1.03^{+0.03}_{-0.03}$	$1.03^{+0.03}_{-0.04}$	$1.01^{+0.03}_{-0.03}$	$0.93^{+0.03}_{-0.04}$
$N_{\rm nth}$	$0.40^{+0.04}_{-0.03}$	$0.49^{+0.04}_{-0.04}$	$0.69^{+0.03}_{-0.03}$	$0.75^{+0.05}_{-0.05}$	$0.78^{+0.05}_{-0.04}$	$0.82^{+0.06}_{-0.06}$
flux$_{\rm disk}$[a] ($\times10^{-9}$)	4.1 ± 0.1	4.0 ± 0.1	4.2 ± 0.1	3.8 ± 0.1	4.0 ± 0.2	3.8 ± 0.3
flux$_{\rm comp}$ ($\times10^{-8}$)	1.12 ± 0.01	1.51 ± 0.02	1.94 ± 0.02	2.04 ± 0.02	1.90 ± 0.02	1.65 ± 0.02
Total flux ($\times10^{-8}$)	2.8 ± 0.4	3.0 ± 0.4	3.9 ± 0.5	3.7 ± 0.4	3.5 ± 0.7	3.2 ± 0.8
χ^2/dof	689/649	682/629	691/629	687/629	664/627	577/598
Derived parameters						
Disk Radius (km)	45 ± 8	36 ± 5	46 ± 7	44 ± 10	41 ± 8	55 ± 16
y parameter	1.5 ± 0.4	0.9 ± 0.4	0.7 ± 0.4	0.6 ± 0.4	0.4 ± 0.8	0.3 ± 0.6
Optical depth (τ)	7.1 ± 1.0	5.0 ± 1.2	4.2 ± 1.3	3.8 ± 1.3	2.6 ± 2.8	2.6 ± 2.2
Seed photon radius (km)	11.4 ± 1.7	11.5 ± 1.6	14.0 ± 1.9	14.7 ± 2.1	16.1 ± 4.7	18.0 ± 4.0

Notes. The model used for fitting is tbabs*(diskbb+nthComp).
[a] All flux calculated in the 0.3–50 keV energy band.

by D. J. Christian & J. H. Swank (1997). The sources that do exhibit dips typically have an inclination greater than 70°. Similar assumptions have been considered in the past for this source (Y. Bhulla et al. 2019; P. Chiranjeevi & K. Sriram 2022).

The optical depth is found from the photon index, assuming a spherical geometry and uniform density for the corona. It can be found out from spectral fitting using the below equation A. A. Zdziarski et al. (1996):

$$\Gamma = -\frac{1}{2} + \sqrt{\frac{9}{4} + \frac{1}{\frac{kT_e}{mc^2}(1+\frac{\tau}{3})\tau}}, \quad (4)$$

where Γ is the photon index and kT_e is the electron temperature in the plasma. We estimate τ for each segment and see a decreasing trend as the source moves along HB, as shown in Figure 5.

The `cflux` model was used to calculate the unabsorbed flux for both the disk and Comptonization component in the energy range 0.3–50.0 keV, and the variation in flux for both components as the source moves along the Z-track is plotted in Figure 5.

We calculated the equivalent seed photon emission area, which is done by equalizing the bolometric luminosity of the soft photons to that of a blackbody with a temperature of $kT_{\rm bb}$

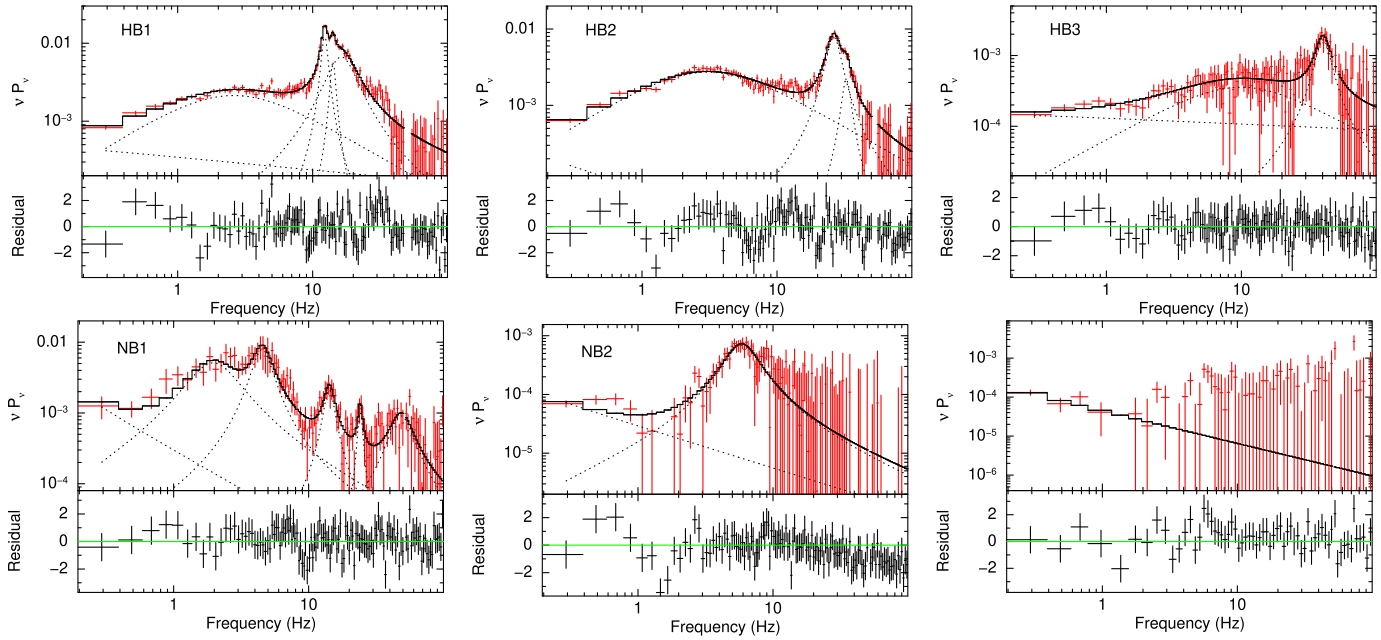

Figure 4. PDS in the HB and NB segments showing QPO features. The PDS is modeled using power-law and multiple Lorentzian functions.

and a radius of $R_{\rm bb}$ (J. J. M. in 't Zand et al. 1999):

$$R_{\rm bb} = 3 \times 10^4 \sqrt{\frac{f_{\rm bol}}{1+y}} \Big/ (kT_{\rm bb})^2, \quad (5)$$

where y is the Comptonization parameter given by $y = 4kT_e/m_ec^2$, $f_{\rm bol}$ is the bolometric luminosity of the source in the unit erg^{-1} m^2 s^{-1}, and d is the distance to the source in kpc. The average value of R_W thus obtained is ∼14 km, and it also shows an increasing trend from HB to NB.

4.2. Spectral Behavior of the Source

The broadband spectrum of the source in the energy range of 0.7–20 keV was modeled using a disk blackbody and a thermal Comptonization model. The unabsorbed flux of the Comptonization and disk blackbody components was computed using the `cflux` command for all segments in the HID. At the beginning of the observation, GX 5-1 was in the HB. As the source goes to the hard apex (HA), the Comptonization flux increases along the HB. The flux then decreases as it moves through the NB. To understand the spectral evolution of the source along the Z-track, we plot the inner disk temperature ($kT_{\rm in}$), electron temperature (kT_e), the inner radius of the disk, and optical depth as a function of different positions in the HID. These parameters were derived from the spectral fitting done in all segments of HID. The variation of the parameters is shown in Figure 5. The electron temperature kT_e of the corona and the Γ increase along HB. kT_e increases from ∼3.82 keV in HB1 to ∼6.12 keV in NB3. During this phase of the evolution from HB to HA, we see that the optical depth of the corona (τ) decreases. The evolution of the source from HA to NB is associated with a decrease in the blackbody temperature ($kT_{\rm bb}$). No clear trend in the variation of inner disk radius was seen during the evolution of the source.

4.3. Temporal Behavior of the Source

We investigate the presence of QPOs in the PDS generated for all segments in the HID. We found the presence of HBOs in all segments of the HB (HB1, HB2, and HB3) and NBOs in two segments (upper and middle NB). No oscillation feature is found in the lower NB. In the extended section of the HB (HB1), we observe HBO at ∼14.12 Hz, and the frequency increases to ∼40 Hz as the source moves along the HB in the Z-track. NBOs are detected at ∼5 Hz in two segments, with QPO frequency showing an increasing trend toward the soft apex. PDSs generated in all the HID segments are modeled using multiple Lorentzian functions as shown in Figure 4; the frequency, width, and amplitude of the QPO signal along with the rms amplitude and maximum frequency are reported in Table 1. The QPO seen in the segments HB1 and HB2 had a shoulder-like component on the high-frequency side. The complete feature was modeled using a combination of two Lorentzians. In NB1, along with the QPO at 4.45 Hz, additional peak features at ∼14 Hz and ∼24 Hz and a broad feature at ∼48 Hz are observed in the PDS.

5. Discussion

This work reports the results obtained from a detailed spectral and timing analysis of the neutron star LMXB source GX 5-1 using AstroSat observations. We investigate the spectral and temporal evolution of the source as it traces the Z pattern in the HID. During the observations, the source traced a complete HB and NB. The broadband spectra in the range of 0.7–20 keV could be well modeled using a combination of a multicolor disk blackbody model and a Comptonization model. We observed the presence of QPOs in HB and NB of the Z-track with increasing QPO frequency in HB toward the HA. The variation of the spectral parameters and their association with the QPO properties are also studied.

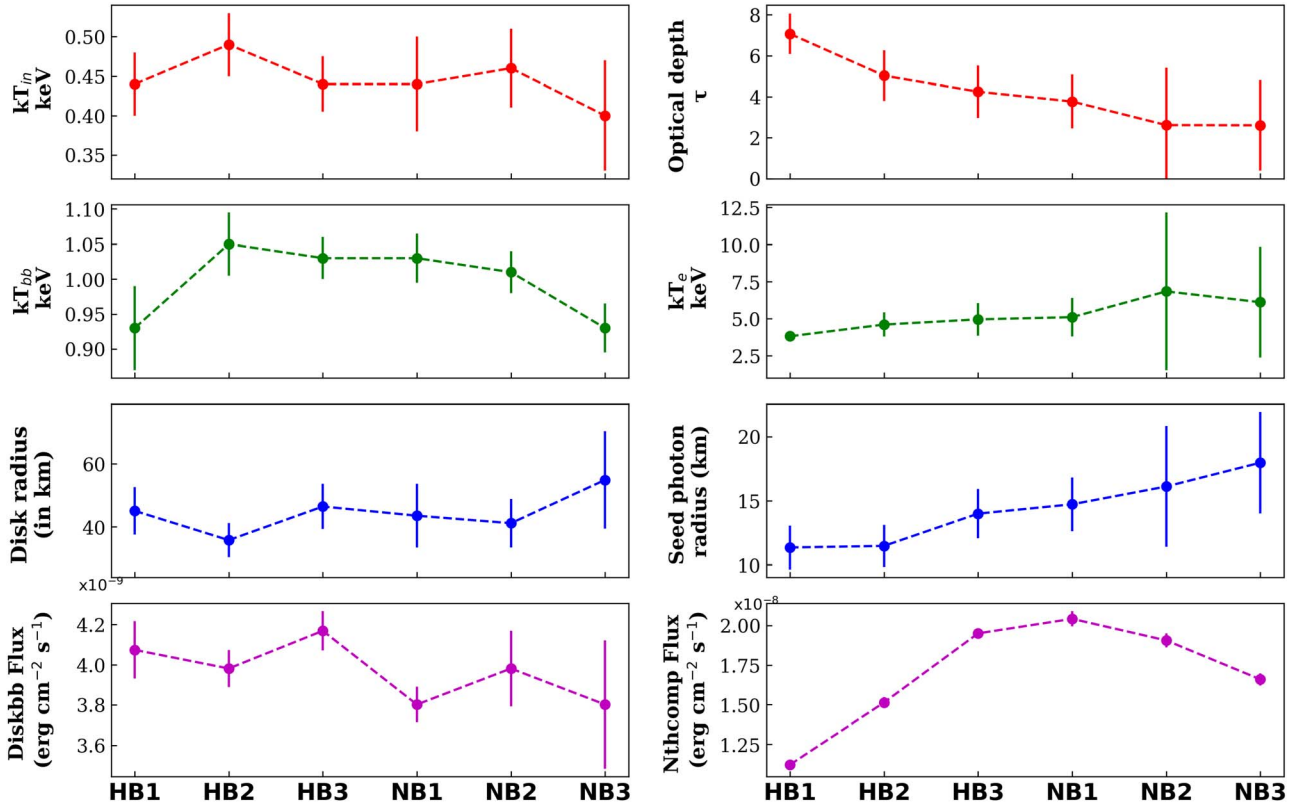

Figure 5. The evolution of spectral parameters from the XSPEC model `tbabs(diskbb+nthComp)` for the SXT and LAXPC combined spectral modeling of GX 5-1. The flux depicted in figure is the unabsorbed flux calculated using the `cflux` model in XSPEC in the energy range 0.3–50 keV.

5.1. Evolution of Spectral Properties

We attempt to understand the origin of Z-track evolution in the source GX 5-1 using spectral analysis done with the simultaneous AstroSat/SXT and LAXPC observations. We considered two different approaches to study the spectral behavior of the source by modeling the source spectrum in the 0.7–20.0 keV. Out of the two models, the source spectrum could be well fitted using a combination of a multicolor disk blackbody model to describe the emission from the accretion disk and a thermal Comptonization model for emission from the corona.

The inner disk temperature remains almost constant throughout the Z-track varying from 0.40 to 0.49 keV. No systematic variation or clear trend is observed in the case of disk radius, which has an average value of ∼45 km. However, we observe that an increase in the disk inner radius corresponds to a decrease in the inner disk temperature, which is expected. We see that, along the HB, disk parameters remain almost constant as the source evolves, considering the temperature, disk inner radius, and disk flux. However, certain parameters related to Comptonization, such as the Comptonization flux, exhibit an increasing trend, while the optical depth of the corona shows a decreasing trend, as illustrated in Figure 5. The Comptonization flux increases along the HB, reaching its maximum value before it starts to decrease along the NB. In the HB, it shows a positive correlation with the electron temperature of the corona. The optical depth (τ) of the corona is found to decrease along the HB and along the NB (∼7.07 in HB1 to ∼2.61 in NB3), which is consistent with the behavior exhibited by GX 17+2 (V. K. Agrawal et al. 2020). This behavior of the source could be described in terms of an increasing accretion rate scenario as presented in V. K. Agrawal & P. Sreekumar (2003). An increase in the soft photon supply to the corona results in the cooling and settling down of a part of the material from the corona onto the disk. This can result in the reduction of the optical depth of the corona. The seed photon radius calculated from the best-fit values shows an increasing trend as the source evolves from HB to NB from ∼11.35 km in HB1 to ∼17.97 in NB3. The average value is 14 km, which is much shorter than the inner disk radius observed in any segment of the HID. This indicates that the seed photons are emitted from a region much closer to the neutron star's surface.

The absence of systematic variation observed in the disk parameters suggests that the source movement along the Z-track could be driven by the variation in the corona or boundary layer and not primarily by the change in mass accretion rate. This result is in agreement with that of J. Homan et al. (2002) and D. Lin et al. (2012). The optical depth decreases along the HB, which is associated with an increase in the Comptonization flux. However, the disk flux remains constant. As the source moves toward the NB, some portion of the corona cools and settles down onto the disk, causing the optical depth to decrease. At the same time, the other portion of the corona is hotter than before, causing a rise in the coronal temperature. In the NB, the optical depth continues to decrease, followed by a decrease in the Comptonization flux, which drives the source evolution along the NB.

5.2. Evolution of Timing Properties

All the segments in the HID, except NB3, show QPOs in the PDS. We observe HBO with frequencies in the range of

13–40 Hz. Y. Bhulla et al. (2019) have reported QPOs at ∼50 Hz in this source using AstroSat data. These observed frequencies are in the expected frequency ranges for Z sources (J. van Paradijs et al. 1988). The HBO frequency increases as the source moves along the HB toward the HA. This frequency change in HB is associated with a decrease in the strength of the HBO. The HBOs and NBOs are observed only in the hard energy (>5 keV) band, which is consistent with previous studies showing that the fractional rms increases with energy (J. van Paradijs et al. 1988; P. G. Jonker et al. 2000). This indicates that the HBOs and NBOs have a stronger contribution from the Comptonizing corona. This behavior is similar to what was observed for the Z source GX 334+0 (Y. Bhargava et al. 2023).

We attempt to explain the observed QPO frequencies using the Lense–Thirring precession model (A. Ingram et al. 2009), where the observed LF QPOs in black hole and neutron star systems are attributed to the misalignment of the inner hot accretion flow with the compact object spin. The frequency of the LF QPOs is given by Equation (2) from A. Ingram et al. (2009):

$$\nu_{\rm prec} = \frac{(5-2\zeta)a(1-(r_i/r_o)^{1/2+\zeta})}{\pi(1+2\zeta)r_o^{5/2-\zeta}r_i^{1/2+\zeta}[1-(r_i/r_o)^{5/2-\zeta}]}\frac{c}{R_g}, \quad (6)$$

where the mass distribution of the hot flow near the compact object is parameterized by ζ; r_i and r_o are the inner and outer radii of the hot flow, respectively; and a is the spin parameter. According to the simulation performed by P. C. Fragile et al. (2007), ζ can be equated to zero for black holes and can also be used for neutron star sources. This scenario may lead to an increased concentration of the accretion flow on the neutron star's surface as the accretion rate increases. To compute the precision frequency, the outer radius of the inner hot flow was kept at the inner disk radius $R_{\rm in}$ obtained from spectral analysis. The outer radius was calculated for the observed QPO frequencies. The model could predict the QPO frequencies observed in HB (13.56, 26.49 Hz); however, it failed to predict any QPOs above 26 Hz using the given parameters due to the larger inner disk. The model could not explain the observed QPO in the HB3 with a centroid frequency of 40 Hz.

We observe NBOs with a frequency ∼5 Hz in two of the segments considered for analysis. In NB1, along with NBO at ∼4 Hz, we observe other QPO features at ∼14 Hz and ∼24 Hz and a broad feature at ∼48 Hz. The origin of these features is not understood. A model for NBO was proposed by L. G. Titarchuk et al. (2001), in which the NBOs are considered as viscous oscillations of a spherical shell around the neutron star surface. The spherical shell viscous frequency $\nu_{\rm ssv}$ is given by

$$\nu_{\rm ssv} = \frac{f\nu_s}{L}, \quad (7)$$

where L is the size of the viscous shell, and f can be 0.5 and $1/(2\pi)$ for the stiff and free boundary conditions in the transition layer, respectively. ν_s is the sonic velocity that is estimated based on Equation (3) from G. Hasinger (1987):

$$\nu_s = 4.2\times10^7 R_6^{-1/4}\left(\frac{M}{M_\odot}\frac{L}{L_{\rm edd}}\right)^{1/8}\ {\rm cm\ s^{-1}}, \quad (8)$$

where R_6 is the radius of the neutron star in units of 10^6 cm. For calculations, we consider a radius of 10 km and a mass of 1.4 $M_\odot$ for the neutron star. We estimate L_s to be 32 km for an NBO frequency of 6 Hz. This value is found to be greater than the calculated seed photon radius in NB. The inner region between the accretion disk, with an average inner radius of 45 km, and the NS surface could be hosting a boundary layer or a transition shell, whose oscillations can produce the NBO.

Acknowledgments

This work uses data from the AstroSat mission of ISRO archived at Indian Space Science Data Centre (ISSDC). The article has used data from the SXT and the LAXPC developed at TIFR, Mumbai, and the AstroSat POCs at TIFR are thanked for verifying and releasing the data via the ISSDC and providing the necessary software tools. Authors thank GD, SAG, DD, PDMSA, and Director, URSC, for encouragement and support to carry out this research. We have used data and/or software provided by the High Energy Astrophysics Science Archive Research Centre (HEASARC), which is a service of the Astrophysics Science Division at NASA/GSFC and the High Energy Astrophysics Division of the Smithsonian Astrophysical Observatory.

ORCID iDs

V. P. Shyam Prakash https://orcid.org/0000-0002-9767-3927

References

Agrawal, V. K., Nandi, A., Girish, V., & Ramadevi, M. C. 2018, MNRAS, 477, 5437
Agrawal, V. K., Nandi, A., & Ramadevi, M. C. 2020, Ap&SS, 365, 41
Agrawal, V. K., & Sreekumar, P. 2003, MNRAS, 346, 933
Antia, H. M., Yadav, J. S., Agrawal, P. C., et al. 2017, ApJS, 231, 10
Asai, K., Dotani, T., Nagase, F., & Mitsuda, K. 2000, ApJS, 131, 571
Belloni, T., Psaltis, D., & van der Klis, M. 2002, ApJ, 572, 392
Bhargava, Y., Bhattacharyya, S., Homan, J., & Pahari, M. 2023, ApJ, 955, 102
Bhulla, Y., Misra, R., Yadav, J. S., & A Jaaffrey, S. N. 2019, RAA, 19, 114
Bradt, H., Naranan, S., Rappaport, S., & Spada, G. 1968, ApJ, 152, 1005
Capitanio, F., Gnarini, A., Fabiani, S., et al. 2023, ARep, 67, S151
Chiranjeevi, P., & Sriram, K. 2022, MNRAS, 516, 2500
Christian, D. J., & Swank, J. H. 1997, ApJS, 109, 177
Clark, G. W. 2018, ApJ, 852, 121
Fabiani, S., Capitanio, F., Iaria, R., et al. 2024, A&A, 684, A137
Fiocchi, M., Bazzano, A., Ubertini, P., & Zdziarski, A. A. 2007, ApJ, 657, 448
Fisher, P. C., Jordan, W. C., Meyerott, A. J., Acton, L. W., & Roethig, D. T. 1968, ApJ, 151, 1
Fragile, P. C., Blaes, O. M., Anninos, P., & Salmonson, J. D. 2007, ApJ, 668, 417
Hasinger, G. 1987, A&A, 186, 153
Hasinger, G., & van der Klis, M. 1989, A&A, 225, 79
Homan, J., Steiner, J. F., Lin, D., et al. 2018, ApJ, 853, 157
Homan, J., van der Klis, M., Jonker, P. G., et al. 2002, ApJ, 568, 878
Homan, J., van der Klis, M., Wijnands, R., et al. 2007, ApJ, 656, 420
in 't Zand, J. J. M., Verbunt, F., Strohmayer, T. E., et al. 1999, A&A, 345, 100
Ingram, A., Done, C., & Fragile, P. C. 2009, MNRAS: Letters, 397, L101
Jackson, N. K., Church, M. J., & Bałucińska-Church, M. 2009, A&A, 494, 1059
Jonker, P. G., van der Klis, M., Wijnands, R., et al. 2000, ApJ, 537, 374
Kuulkers, E., van der Klis, M., Oosterbroek, T., et al. 1994, A&A, 289, 795
Lin, D., Remillard, R. A., Homan, J., & Barret, D. 2012, ApJ, 756, 34
Mitsuda, K., Inoue, H., Nakamura, N., & Tanaka, Y. 1989, PASJ, 41, 97
Mitsuda, K., Inoue, H., Koyama, K., et al. 1984, PASJ, 36, 741
Muno, M. P., Özel, F., & Chakrabarty, D. 2003, ApJ, 595, 1066
Ross, R. R., Fabian, A. C., & Young, A. J. 1999, MNRAS, 306, 461
Shakura, N. I., & Sunyaev, R. A. 1973, A&A, 24, 337
Singh, K. P., Stewart, G. C., Westergaard, N. J., et al. 2017, JApA, 38, 29
Tauris, T. M., & van den Heuvel, E. P. J. 2006, in Compact Stellar X-ray Sources, ed. W. Lewin & M. van der Klis, 39 (Cambridge: Cambridge Univ. Press), 623

Titarchuk, L. G., Bradshaw, C. F., Geldzahler, B. J., & Fomalont, E. B. 2001, ApJL, 555, L45
van der Klis, M. 2000, ARA&A, 38, 717
van der Klis, M. 2004, arXiv:astro-ph/0410551
van der Klis, M., Jansen, F., van Paradijs, J., et al. 1985, Natur, 316, 225
van Paradijs, J., Hasinger, G., Lewin, W. H. G., et al. 1988, MNRAS, 231, 379
White, N. E., Stella, L., & Parmar, A. N. 1988, ApJ, 324, 363
Wijnands, R., Méndez, M., van der Klis, M., et al. 1998, ApJL, 504, L35
Wilms, J., Allen, A., & McCray, R. 2000, ApJ, 542, 914
Zdziarski, A. A., Gierlinski, M., Gondek, D., & Magdziarz, P. 1996, A&AS, 120, 553
Zhang, W., Jahoda, K., Swank, J. H., Morgan, E. H., & Giles, A. B. 1995, ApJ, 449, 930
Zycki, P. T., Done, C., & Smith, D. A. 1999, MNRAS, 309, 561